

Figure 2.8: General view of the EMC polarized target

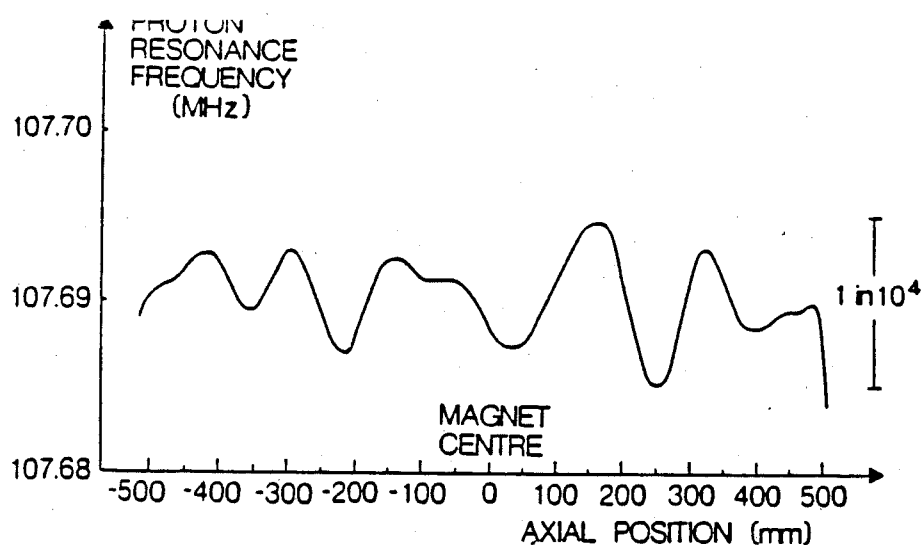


Figure 2.9: Polarized target axial magnetic field. The field uniformity is better than 10^{-4} .

The target material is cooled by a $^3\text{He}/^4\text{He}$ dilution refrigerator [79]. This provides a cooling power of 2 watts at 0.5 K thus safely offsetting the 1.1 watts microwave power which is necessary to polarize the protons. A dilution refrigerator was chosen due to the good heat contact between the target material and the dilute solution, and the good convection heat transfer in the dilute solution itself. When the target was operated in "frozen spin" mode [80] with the microwaves switched off, temperatures of 130 mK were attained for a polarization decay rate of $0.78 \pm 0.1\%$ per day

The polarization is measured by four NMR coils buried in the target material of each section. Each coil is in the form of a single turn loop of 2 mm diameter cupro-nickel tube. The loops are teflon coated to reduce the non-uniform sampling in the high field close to the surface of the coils and are uniformly mounted along each section with their axes perpendicular to the beam direction. The NMR system is calibrated using the thermal equilibrium signals in the region of 1 °K. These temperatures were attained with only ^4He circulating in the target and measured using a calibrated germanium resistor and three Speer carbon resistors.

Important operational parameters were continuously monitored by a single crate CAMAC system. When preset limits were overpassed the alarm system started an audible alarm in the experiment counting room and generated an automatic call on the CERN paging system. The modem was linked to a standard telephone line so that a remote operator, equipped with a portable hard-copy terminal and an acoustic coupler could access the polarized target information and

Chapter 5

The Extraction of Asymmetries from the Data

5.1 Mathematical considerations

This first section develops the mathematics used to extract the asymmetry for each individual period. The important features of cancellation of beam fluxes and target masses are discussed, together with the influence of the spectrometer acceptance. Finally, the equation that relates the measured yields to the physics asymmetry is derived.

5.1.1 Expected Number of Events from Each Target Cell

The polarized target cells contain four different kinds of nuclei, H, N, He and Cu, in the form of frozen ammonia beads, liquid helium for refrigeration purposes and copper NMR coils. For a target half with a polarization parallel to that of the beam the total number of events N^+ recorded in a given kinematic Q^2 - ν bin can be expressed in terms of the nuclear cross-sections and the total number of nuclei present in the cell (respectively $\sigma_p, \sigma_N, \sigma_{He}, \sigma_{Cu}$, and N_p, N_N, N_{He} and N_{Cu}) through

$$N^+ = F a(Q^2, \nu) \Delta Q^2 \Delta \nu \left[N_N \sigma_N + N_{He} \sigma_{He} + N_{Cu} \sigma_{Cu} + P_b P_t N_p \sigma_p^+ + (1 - P_b P_t) N_p \sigma_p^- \right] \quad (5.1)$$

Here F is the total integrated flux during the time interval of data taking, $a(Q^2, \nu)$ is the acceptance of the target half, σ stands for the double differential cross-section for scattering on unpolarized nuclei, $d^2\sigma/dQ^2 d\nu$, and σ^+ corresponds to the scattering when the muon and proton polarizations are parallel. The coefficients P_b and P_t are the target and beam polarizations respectively. An addi-

tional term arising from the polarization of the spin-1 nitrogen nucleus has been neglected; its effect will be introduced later in section 5.3.1 as a correction. The equation above can be rewritten

$$N^{\dagger} = F a(Q^2, \nu) \Delta Q^2 \Delta \nu M \sigma \left[1 + f P_b P_t \frac{\sigma_p^{\dagger} - \sigma_p}{\sigma_p} \right] \quad (5.2)$$

where the following notation has been introduced

$$M \sigma \equiv N_p \sigma_p + N_N \sigma_N + N_{He} \sigma_{He} + N_{Cu} \sigma_{Cu} \quad (5.3)$$

$$f \equiv \frac{N_p \sigma_p}{N_p \sigma_p + N_N \sigma_N + N_{He} \sigma_{He} + N_{Cu} \sigma_{Cu}}$$

The coefficient f , named the "proton dilution factor" is related to the fraction of free polarizable protons in the target. The product $M \sigma$ corresponds to the total cross-section, and since it depends on the amount of material in each target cell it will be different for the upstream and downstream halves.

Equation (5.2) can be given a final form by introducing the cross-section asymmetry $A = (\sigma^{\dagger} - \sigma^{\dagger})/(\sigma^{\dagger} + \sigma^{\dagger}) = (\sigma - \sigma^{\dagger})/\sigma$. Then we have

$$N^{\dagger} = F M \sigma a \Delta Q^2 \Delta \nu (1 - f P_b P_t A) \quad (5.4)$$

For the case when the target and beam polarizations are antiparallel, an equivalent expression can be obtained for N^{\dagger} replacing the minus sign by a plus in the last term. Equation (5.4) will be used in the next section to obtain an expression for the physics asymmetry in terms of the measured yields N_i .

5.1.2 Extraction of the Asymmetry for a Single SPS Period

The arrangement of a typical period is depicted in Figure 5.1. Data taking commences with the two cells of the target polarized in opposite directions with absolute values P_1 and P_2 . After a total flux F_1 has passed through the target, the polarizations in the two cells are reversed and data is taken in the new configuration until a further flux F_2 has passed through the system. The absolute values of the polarizations after the reversal will in general differ from the previous ones and are denoted as P_3 and P_4 .

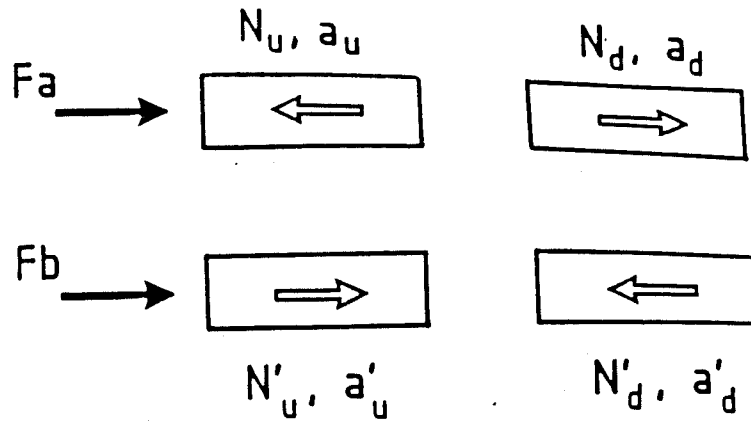


Figure 5.1: The target arrangement of a typical SPS period

Equation (5.4) can be applied separately for each of the four cases. The number of events counted in a given Q^2 - x bin before the polarization reversal from the upstream and downstream cells will be denoted as N_u and N_d respectively, and the corresponding yields after the reversal as N'_u and N'_d . With the specific polarization orientations of Figure 5.1 we have

$$\begin{aligned}
 N_u &= F_1 M_1 \sigma a_u \Delta Q^2 \Delta v (1 + f P_b P_1 A) \\
 N_d &= F_1 M_2 \sigma a_d \Delta Q^2 \Delta v (1 - f P_b P_2 A) \\
 N'_u &= F_2 M_1 \sigma a'_u \Delta Q^2 \Delta v (1 - f P_b P_3 A) \\
 N'_d &= F_2 M_2 \sigma a'_d \Delta Q^2 \Delta v (1 + f P_b P_4 A)
 \end{aligned} \tag{5.5}$$

Two different values M_1 and M_2 are used to account for the different number of nucleons in each target cell. On the other hand, four distinct acceptances a_i are introduced to allow for the possible variation either in space (both target halves) or in time (before and after the reversal). The two integrated fluxes F_1 and F_2 can be very different as they depend on the total number of days of data taking for each polarization orientation. Their values can be determined from the T10 events (section 2.4.6) with a precision not better than 1%. This accuracy is not enough for the purpose of this experiment and therefore they have to be considered as unknowns, on the same footing as the total number of nucleons M_i and the four acceptances a_i .

In the set of equations appearing in (5.5) it is necessary to extract the asymmetry A from the four measured numbers N_i . The unknown beam fluxes and target masses cancel if the following specific combination of the four yields is taken

$$\frac{N_u N'_d}{N_d N'_u} = \frac{a_u / a_d}{a'_u / a'_d} \frac{(1 + m_1 A)(1 + m_4 A)}{(1 - m_2 A)(1 - m_3 A)} \quad (5.6)$$

where $m_i \equiv f P_i P_i$. Remark that the acceptances have not disappeared but enter in a specific combination which we shall define as the κ factor

$$\kappa \equiv \frac{a_u / a_d}{a'_u / a'_d} \quad (5.7)$$

For the case when κ has a value of 1 the acceptance effects cancel out, and eq(5.6) expresses the desired asymmetry in terms of known quantities. From the Monte Carlo calculations presented in section 4.5 we know that the acceptance of the upstream cell of the target, a_u , is of the order of 4% larger than that of the downstream, a_d , thus a_u/a_d is ~ 1.04 . Since a'_u/a'_d represents the same ratio after the polarization reversal, for a stable apparatus would expect $a_u/a_d \approx a'_u/a'_d$ which amounts to stating $\kappa \approx 1$. The factor κ would only depart from unity if the acceptance ratio is itself time dependent, and such variations are expected to be much smaller than the separate ratios a_u/a_d . Section 5.4 discusses in greater depth from a quantitative point of view the effect of acceptances on the measured asymmetry.

In order to express the asymmetry A in terms of measured quantities and the factor κ , it is useful to introduce the raw asymmetries Δ_1 and Δ_2 :

$$\Delta_1 = \frac{N_u - N_d}{N_u + N_d} \quad \Delta_2 = \frac{N'_u - N'_d}{N'_u + N'_d} \quad (5.8)$$

Each of the two Δ 's would be proportional to the asymmetry A if the acceptances and masses of both halves of the target were equal. If we didn't have the facility to reverse the sense of polarization, that would be our best approximation to the final result. However, combining Δ_1 and Δ_2 one gets rid of the separate masses of the targets; leaving aside the mathematical details (these can be found in Ref. [115]), it is possible to show that to first order in $\kappa - 1$:

$$A = \frac{1}{\bar{m}} \left[\frac{\Delta_1 + \Delta_2}{2} - \frac{\kappa - 1}{4} \right] \quad (5.9)$$

where \bar{m} is defined as the average of the four separate values

$$\bar{m} \equiv \frac{1}{4} (m_1 + m_2 + m_3 + m_4)$$

Taking for the moment $\kappa = 1$, and defining a global raw asymmetry Δ as the average of Δ_1 and Δ_2 we obtain

$$\Delta = P_b P_t f A \quad (5.10)$$

Equation (5.10) will be the basis of the extraction of the asymmetries for each period. In the calculations that follows the assumption $\kappa = 1$ will be made throughout, the effect of the acceptance being introduced in section 5.4 as a systematic error.

5.2 Calculation of the Asymmetries

This section presents the results obtained for the asymmetries using the equations developed in the previous pages. The total data sample corresponds to 11 running periods at three different beam energies 100, 120 and 200 GeV. Table 5.1 summarizes the running conditions and number of events for each of them. A period corresponds to several days of data taking and it usually coincides with an SPS cycle. It always includes one polarization reversal, with the sole exception of P2A85. In order to treat it on the same footing as the others, it was merged with a fraction of data from a nearby period of the same energy and opposite polarization (P2C85). Whenever an SPS cycle comprised two polarization reversals, the corresponding period was split into two which were subsequently treated independently. This was the case of P2C84, P3C84 and P2B85. The following subsections describe how the asymmetries were calculated separately for each of these periods and then merged together. First the criteria for selecting events are discussed, followed by an account of the determination of the factors entering in eq(5.10), that is the beam and target polarizations and the proton dilution factor f , the fraction of polarizable protons in the sample. Finally the results are

presented and compared with previous measurements.

Table 5.1: Summary of running conditions

Period	Energy (GeV)	Initial P_T orientation	Events after cuts
2B84	200	-/+	114.6 k
2C84 I	200	-/+	65.5 k
2C84 II	200	+/-	68.7 k
3A84	120	-/+	236.3 k
3B84	200	+/-	115.8 k
3C84 I	200	-/+	44.0 k
3C84 II	100	+/-	202.1 k
2A85	100	-/+	41.5 k
2B85 I	120	-/+	180.5 k
2B85 II	200	+/-	58.5 k
2C85	200	-/+	97.5 k

5.2.1 Event Selection Criteria

Not all events with a fully reconstructed muon were used in the asymmetry analysis. A number of cuts were applied to improve the quality of the data, to remove regions of varying acceptance or to increase the vertex resolution. These cuts are described below and summarized in Table 5.2.

Kinematic cuts

The following five kinematic cuts were applied to the data

- a low Q^2 cut
- a low θ cut
- a low v cut

- a high y cut
- a low E'_μ cut

The low Q^2 and scattering angle θ cuts have the purpose of removing the central region of the spectrometer where the trigger response is low and the acceptance varies substantially due to the inefficient regions around the chamber centers. In addition the θ cut eliminates the events for which the vertex resolution is the poorest (see section 4.3).

The kinematic variable ν is calculated from the measured incident and outgoing muon energies ($\nu = E - E'$). When E is close in value to E' , ν is obtained as the difference of two big numbers and has in consequence a rather large error. The low ν cut is introduced to remedy this situation by imposing a minimum acceptable difference between E and E' .

In section 5.3 it will be shown that radiative corrections are most important in the high y range. A cut of $y < 0.85$ was therefore found necessary in order to avoid the regions where these corrections became too large.

Finally, the scattered muon energy cut, E' , removes events in the region where the fraction of muons from π/K decay is considerable. A study has shown that at low E' the reconstructed outgoing muon might actually be a decay particle, while the genuine scattered μ passes undetected through the central deadened chamber regions. The beam hodoscope H5 was used to search for high energy low angle μ 's, and it was found that the contamination is negligible for E' above 15% of the beam energy.

Table 5.2: Cuts applied to the data

E_μ (GeV)	Q^2_{min} (GeV/c) ²	Θ_{min}	ν_{min} (GeV)	y_{max}	E'_{min} (GeV)
100	1.5	1°	10	0.85	15
120	2.0	1°	10	0.85	18
200	3.0	1°	20	0.85	30

Figure 5.2 shows the profile of vertex distributions along the beam axis together with the physical limits of each of the two halves. Taking into account that the density of material inside the target is much more important than outside it, it is clear that a large fraction of the events lying beyond the cell ends are actually genuine target events. This is confirmed by the Monte Carlo simulation of the experiment in terms of the smearing caused by the finite resolution of the spectrometer (section 4.3). In order to maximize the total available statistics the fiducial target cuts were then placed outside the actual limits of the target sections, 5 cm beyond the upstream and downstream ends and 2 cm towards the center. The central cuts are more conservative in order to prevent events from one half to be assigned to the other. The resultant limits are shown in Figure 5.2. The small correction introduced by the events accepted within the cuts, but that actually originate outside the cell material, is discussed in section 5.3

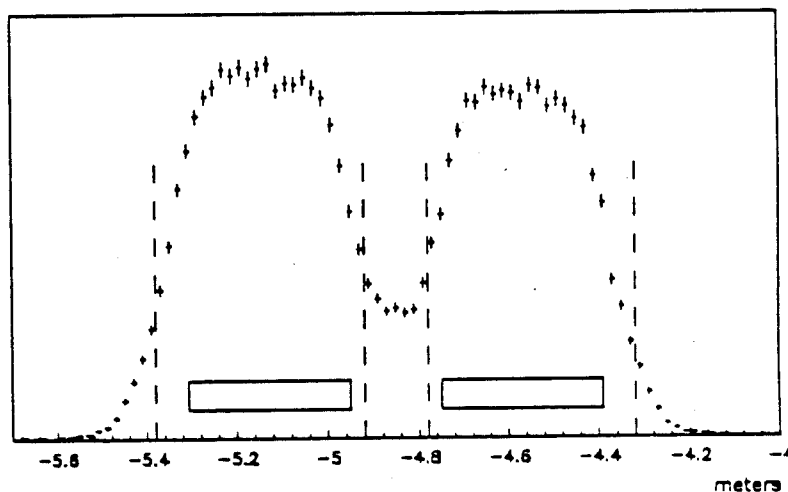


Figure 5.2: Definition of the longitudinal vertex cuts

Smearing effects in the plane perpendicular to the target axis are on the other hand much less important. In addition, the extra material beyond the cell volume is no longer negligible due to the presence of several thick copper rings which hold each target half in position. The cross sectional cuts are therefore placed *within* the cell volume, 3 mm from the mylar wall. Since the target is not cylindrical (see Figure 2.8), this cut corresponds to accepting events within a 2.7 cm radius but

whose y -coordinate does not exceed 2.2 cm. Table 5.3 shows that due to the smallness of the beam cross-section, this perpendicular cut does not remove many events, as opposed to the $\sim 10\%$ loss registered after imposing the vertex x limits.

Cuts were also placed on the beam tracks to ensure that the same flux traverses both target halves, an important assumption that was made while deriving the equations presented in section 5.1. These include both a cross sectional fiducial region and a maximum slope limit. In addition, beam momentum cuts were applied to remove any remnants beyond the gaussian tails shown in Figure 2.5. Most of these cuts were applied at an early stage in the software reconstruction chain, mainly at the beam processor in Snomux (section 3.1.4).

Table 5.3: Statistics of event losses after applying cuts

Cut Applied	Number of events	Percentage lost
Events reconstructed	1980 k	
Beam Cut	1970 k	0.5%
Q^2 Cut	1670 k	15%
ν Cut	1565 k	6%
y Cut	1475 k	6%
P_{\perp} Cut	1470 k	0.3%
Θ Cut	1355 k	8%
Perpend. Vertex Cut	1345 k	0.7%
Longit. Vertex Cut	1220 k	9%
Fraction of events left		62%

5.2.2 Beam and Target polarizations

The polarization of the muon beam was calculated with the program HALO [116] that simulates the beam transport system. As it is discussed in appendix A, the predictions of the program were found to be in agreement with an early set of measurements of the polarization performed by

an experiment [117] which shared the beam line with the EMC. The results obtained for the three beam working conditions used in this experiment are summarized in Table 5.4. The possible effect of changes in helicity due to the precession of the muon spin in the magnetic fields of the beam line has been considered and found to be negligible [118]. The spin rotation angle with respect to the particle trajectory is given by $\theta = \gamma a \theta_b$, where $\gamma = E_\mu/m_\mu$, $a = (g-2)/2$, the anomalous magnetic moment of the muon and θ_b is the total bending angle. The global effect is very small because the two main 24 mrad vertical bendings compensate each other (Figure 2.3).

Table 5.4: Summary of beam working conditions

E_π/E_μ (GeV)	Polarization	Total Events
110/100	0.77 ± 0.06	603.1 k
130/120	0.79 ± 0.06	416.8 k
210/200	0.82 ± 0.06	202.1 k

The target polarization was monitored continuously throughout the data taking runs by means of eight NMR coils buried in the target material, the values being dumped to tape once per SPS burst. The polarized target processor, at the Snomux level of the analysis chain (section 3.1.4), decoded the relevant information and calculated an average measurement for each coil on a run-by-run basis. This information is read at the final stage of the analysis, where an average is taken of the four coils corresponding to each target half and a global figure is produced by combining all the runs comprising each period. Typical values ranged between 75% and 80%, with an approximate drop of 5% per week when running in frozen spin mode. The reversal of the polarization was always performed during a machine shut-down, and data taking never recommenced until the polarization had reached a value of 65-70%.

5.4.2 Time Dependence of the Acceptances as Extracted from the Data

The number of events recorded from a target half will be dependent not only on the polarized cross-sections we want to measure but also on the acceptance of the respective cell. Different acceptances between both target halves will in principle give rise to false asymmetries. However, it was proved in section 5.1 that these effects cancel thanks to the fact that the polarization direction is reversed once per period, *provided* the ratio a_u/a_d between the upstream and downstream halves is constant. It is therefore essential to study the stability of the different parts of the apparatus and the effects that possible time variations could have on the acceptance ratio. These analyses can be done according to three different but complementary methods as presented below. First, the measurements of the detector efficiencies give some insight regarding apparatus time dependent problems. Second, the data yields can be used to directly compare the ratio of acceptances for different periods. Third, although not employed to determine absolute acceptances, the Monte Carlo can be useful to estimate relative variations and dependences.

Variation of chamber efficiencies

The determination of chamber efficiencies has been described in detail in section 3.3, only the relevant results to the present discussion are recalled here. The time dependence of the detectors' performance is studied by plotting the overall plane efficiencies as a function of run number on a period-by-period basis. Examples of these plots are shown in Figure 3.17. Although most chambers are quite stable, there are clear time effects in the case of the proportional planes P45 and the drift chambers W12 and W45. For P45, abrupt variations took place as a whole plane went on and off. This happened essentially for only two periods, P3B84 when one of the modules took fire and P3C84 in which a timing problem caused a 10% drop in efficiency during the first fifth of the period. On the other hand, the drift chambers W12 and W45 showed a steady decline in their performance all through the 1984 data taking interval. A careful study showed that this variation was due to a decreasing efficiency in the central region. This can be clearly seen in Figure 5.13 which compares the radial efficiency for a W12 plane before and after the polarization reversal for period P2C84. The net effect of this variation can be described as a continuous increase of the radius of the central dead regions of these chambers.

The consequences of the W45 efficiency drop are to a large extent compensated by the presence of the adjacent P45 planes covering its central region. It was precisely for this purpose that they were installed after the NA9 phase of the experiment, as the problems with W45 had already

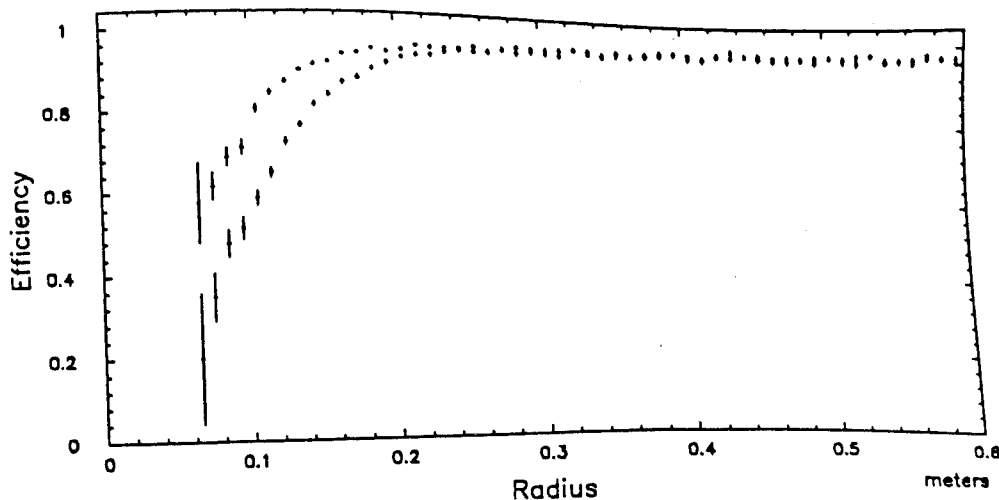


Figure 5.13: Time dependence of the radial efficiency of W12. The two curves correspond to data before and after the polarization reversal.

become apparent. On the contrary, since no other chamber takes over the increasing hole in W12, all events whose scattered muon falls within this region are lost.

How do these changes affect the ratio a_u/a_d ? In section 4.5 Monte Carlo calculations were presented showing that the acceptance of the upstream half of the target is about 4% larger than that of the downstream for the SPS period P3A84. This figure can be qualitatively understood by noticing that muons are lost at low angles due to the central dead regions in the chambers. Since the solid angle subtended from the downstream half is slightly larger than the upstream's, its acceptance will be somewhat lower.

This heuristic interpretation of the Monte Carlo result provides a framework to predict the consequences of chambers decay on the acceptances. In the limit when there are no insensitive areas in the detectors, the quotient a_u/a_d should be very close to one. On the other hand, as the radii of the central beam regions increase, a_u/a_d will differ more and more from unity. One can then expect, on account of the behavior of the efficiencies, that the ratio a_u/a_d will be higher than 1, becoming increasingly larger for subsequent periods. In the next section I will show that this is indeed what it is found from the data.

In section 5.1 it was shown how the four measured yields N_i can be used together to eliminate the dependence on the target masses and beam fluxes. It is possible, on the other hand, to take a second class of combination in which it is the physics asymmetry that cancels. Using the expression for N_i from equation (5.5), it is immediately seen that

$$\frac{N_u \cdot N'_u}{N_d \cdot N'_d} = \left(\frac{M_u}{M_d} \right)^2 \times \frac{a_u a'_u}{a_d a'_d} \cong \left(\frac{M_u}{M_d} \right)^2 \times \left(\frac{a_u}{a_d} \right)^2$$

Since the quotient of cell masses M_u/M_d stays constant all through the experimental run, the chosen combination of the four yields can be directly used to compare a_u/a_d for different periods. Figure 5.14 shows on a period-by-period basis the measured ratio of yields as a function of run number for an energy independent set of kinematic cuts. Except for an overall normalization (which depends on M_u/M_d), we are effectively observing the global behavior of the period averaged acceptance ratios.

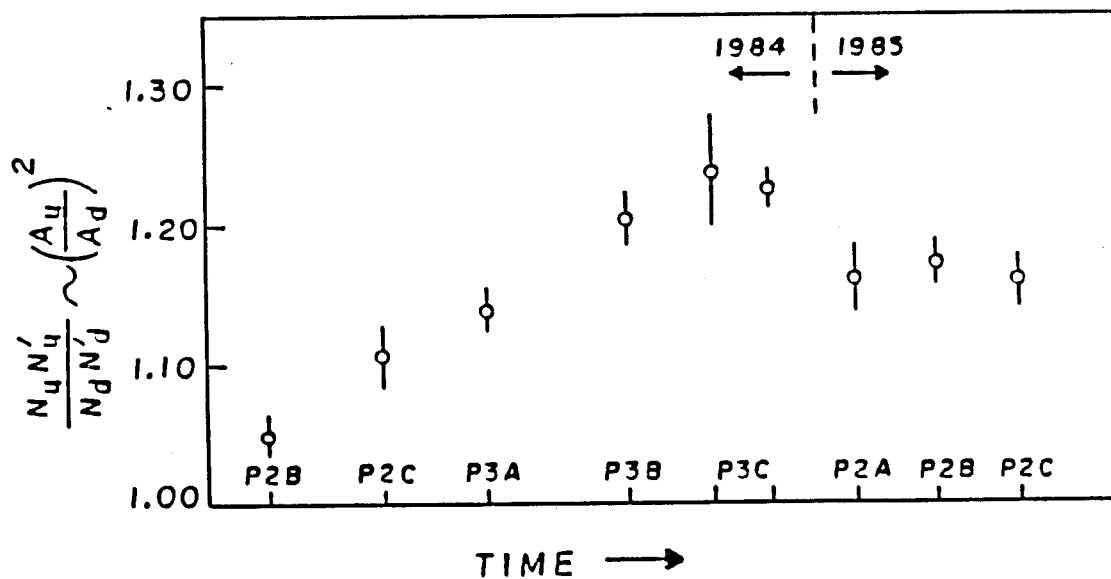


Figure 5.14: Comparison of acceptance ratios for different periods. The quantity plotted is the measured yield ratios $N_1 \cdot N_2 / N_3 \cdot N_4$, which correspond to $(a_u/a_d)^2$ up to a normalization factor.

The tendency of a_u/a_d to increase with time agrees well with the argument presented in the previous section. One can in addition see a break at the start of the 1985 runs, which is likely to originate from the fact that a certain number of chambers were rewired or replaced by spares.

If the reasoning concerning the decay of the wire chambers is correct, the ratio a_u/a_d should not vary significantly if the event sample is restricted to scattered muon tracks that do not traverse the central regions where the efficiency is dropping. This is indeed the case as shown in Figure 5.15 where a cut has been applied to kill all tracks found in P45. This cut not only removes the low angle events, but also eliminates the variations due to P45 planes abruptly dying in the middle of a period. The previous trend to increase has now completely disappeared, confirming that the time dependent effects are localized in an area close to the beam line.

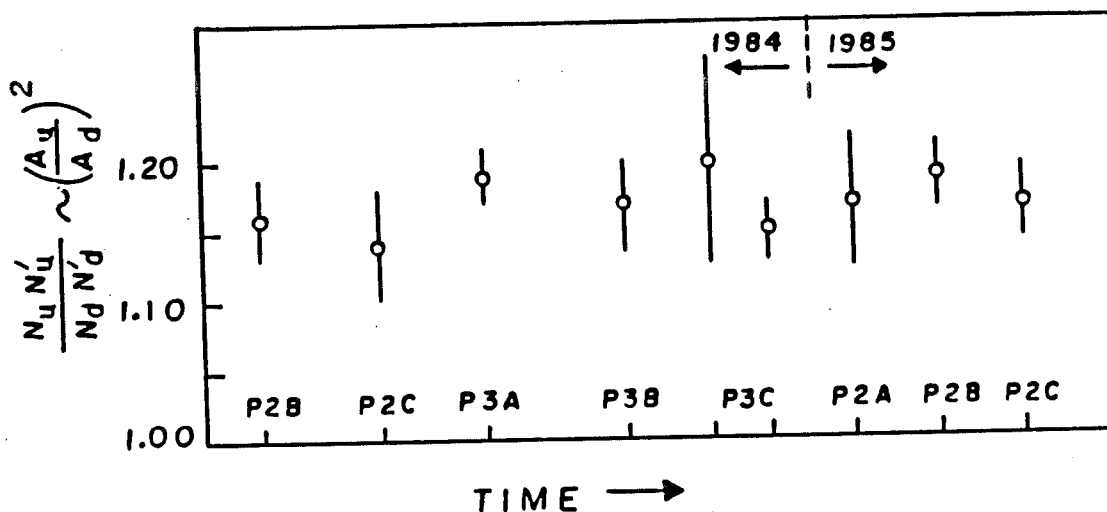


Figure 5.15: Ratio of acceptances for tracks reconstructed outside P45

5.4.3 False Asymmetries Originating from Acceptance Effects

In the previous section it was concluded that the data support a scenario in which a_u/a_d increases uniformly during the 1984 data taking runs. Although unexpected variations can in principle take place within a period, it is then reasonable to assume that $a'_u/a'_d > a_u/a_d$, which means that the factor κ is larger than one.

According to equation (5.9), the physics and the measured asymmetries are related by

$$A_1 = A_1^{meas} \pm \frac{(\kappa - 1)}{4m} \quad (5.21)$$

where $m = f D P_i P_s$. The two signs in front of the last term stand for the two possible initial arrangements of the target polarization orientations. In what follows I will denote as "type 1" periods those with a setup similar to the one shown in Figure 5.1. Contrarywise, "type 2" periods correspond to the case with the target polarizations in the opposite direction. Table 5.1 shows explicitly the correspondent assignments for each period. Since the physics asymmetry does not depend on the data sample under consideration, one gets for the measured values A_{meas} :

$$\begin{aligned} \text{periods type 1:} \quad A_{meas} &= A_1 + \frac{(\kappa - 1)}{4m} \\ \text{periods type 2:} \quad A_{meas} &= A_1 - \frac{(\kappa - 1)}{4m} \end{aligned} \quad (5.22)$$

Given that κ is larger than 1, one can predict that periods type 1 should measure consistently larger asymmetries than type 2 ones. This is indeed found, as it can be appreciated from Figure 5.16 which shows as a function of x the asymmetries obtained when each type of periods are merged together (data shown correspond only to the 1984 runs, errors are only statistical). The black squares (type 1 periods) lie systematically above the open circles (type 2 periods).

A second possible cross-check can be performed by subdividing the data sample in events whose scattered muon is or is not found in P45. If most of the false asymmetries effects originate from changes in the central regions, the measured A values from different periods should be consistent among themselves when the P45 muons are eliminated. Figure 5.17 shows the results separately for type 1 and type 2 periods (the data has been merged into a total of 5 x bins in order to compensate for the reduction in statistics). The tendency observed is as expected. Only the sample of muons found inside P45 show a dependence with the type of period in consideration. In addition for type 1 periods the points shift upwards, and for type 2 periods downwards, as predicted by equation (5.22).

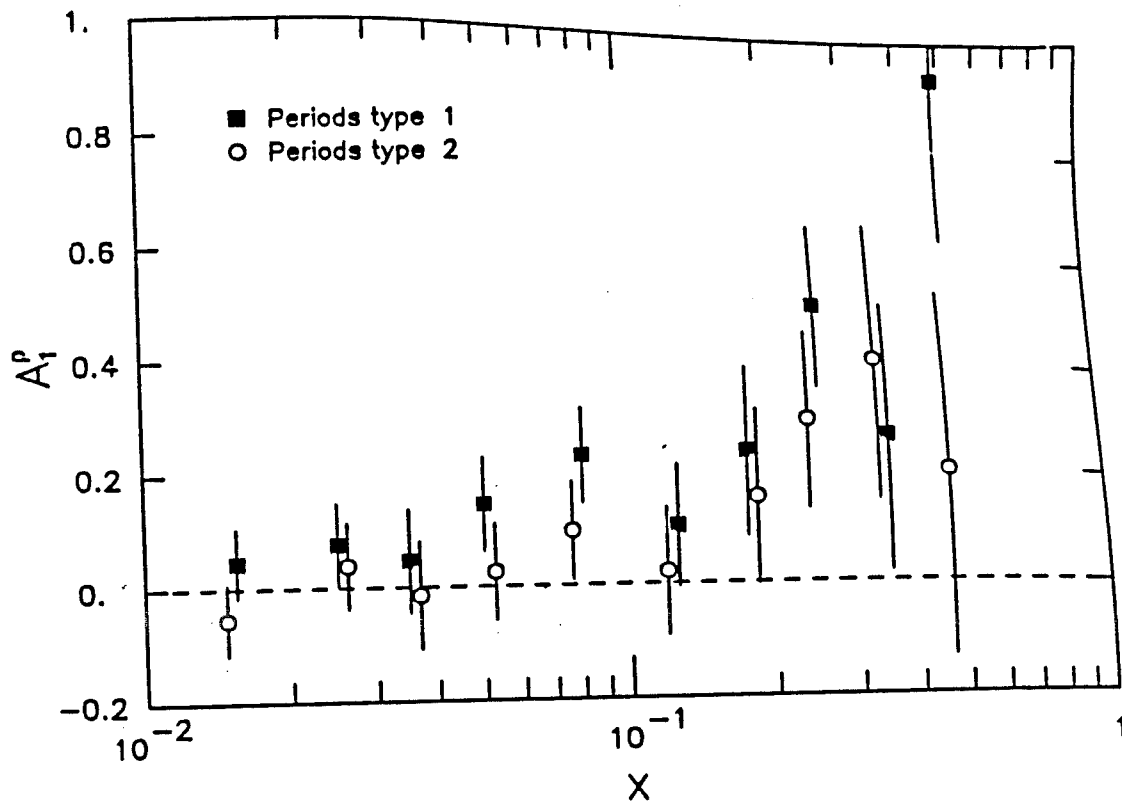


Figure 5.16. Comparison of asymmetries obtained from periods starting with different polarization orientations (see text). Data correspond to the 1984 runs.

5.4.4 Introduction of Acceptance Effects in the Results

The kind of subdivision presented in Figure 5.17 suggests a possible way to estimate the average κ for a group of periods. Let's denote κ_{in} and κ_{out} the κ factors for the event samples whose scattered muons are found respectively inside and outside P45. Since time dependent effects are not important far from the central regions, it is reasonable to assume that the associated value κ_{out} will be very close to one. Let's denote A_{in} and A_{out} the measured asymmetries for each subdivision. Since the physics result should be independent on the data sample, we have for type 1 periods

$$A_1 = A_{in} - \frac{(\kappa_{in} - 1)}{4m} = A_{out} - \frac{(\kappa_{out} - 1)}{4m}$$

and hence

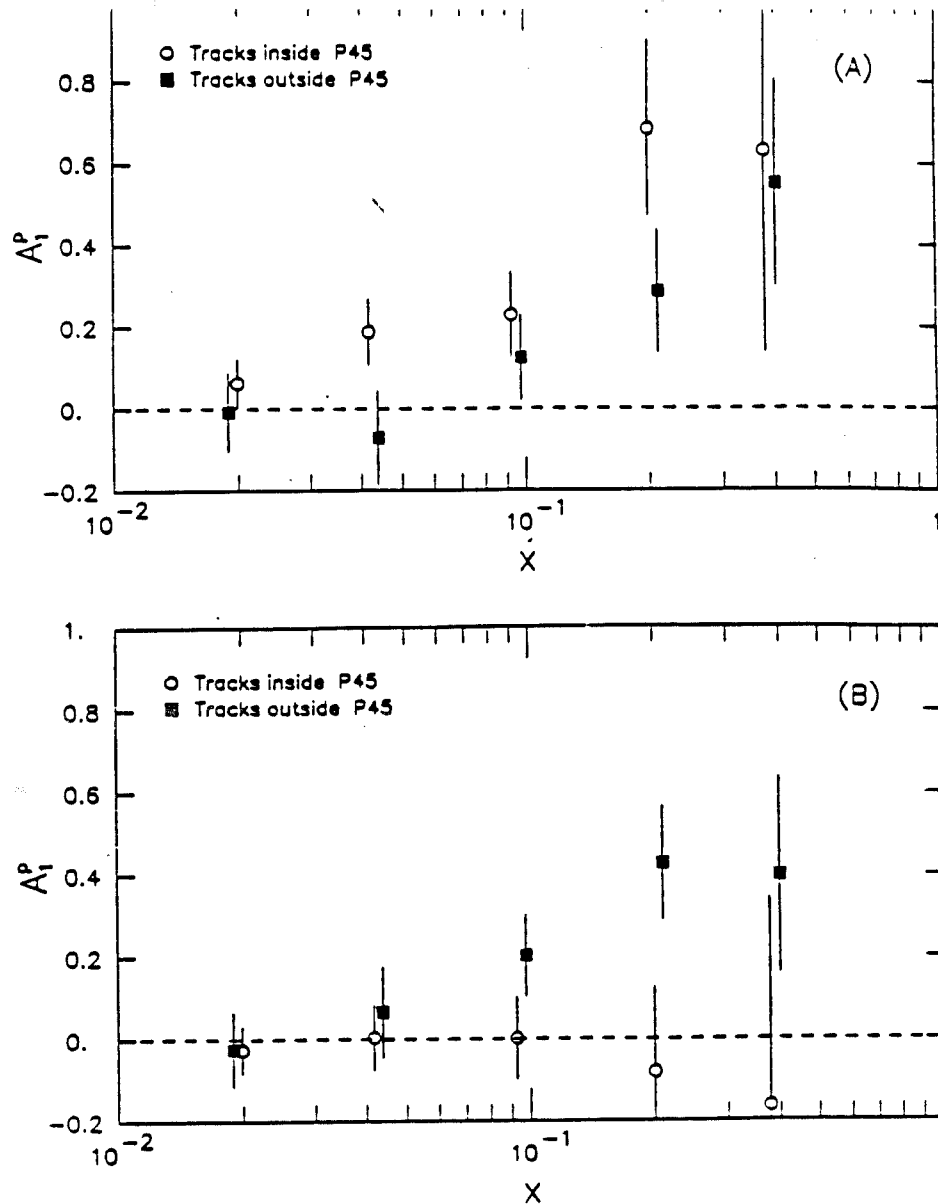


Figure 5.17: Comparison of asymmetries for tracks outside and inside P45. (A) Periods type 1. (B) Periods type 2.

$$\kappa_{in} - 1 = 4m \times (A_{in} - A_{out}) \quad (5.23)$$

and a similar equation with the opposite sign for type 2 periods.

Figure 5.18 shows the values of $4m(A_{in} - A_{out})$ separately for each kind of period as measured from the data. The points lie above and below zero respectively as expected from the fact that

equation (5.23) changes sign for different initial polarization orientations. Given that there is no apparent dependence on the kinematics, we can take a value averaged over the entire x range:

$$\kappa_{in} - 1 = 0.026 \pm 0.012 \quad (\text{type 1 periods}) \quad (5.24)$$

$$\kappa_{in} - 1 = -0.029 \pm 0.012 \quad (\text{type 2 periods})$$

The fact that both values of κ are so similar implies that their effect will to a large extent cancel when the whole 1984 data sample is merged together.

A similar line of argument has not been presented for the 1985 data because there was not a similar apparent smooth behavior of the acceptances. In addition, as it was explained in section 5.2, the first period, P2A85, comprises actually some data that have been extracted from the last one, P2C85 (this was due to the absence of polarization reversal in P2A85). As a consequence, there is not a one-to-one relation between time and period number as there was during the 1984 runs.

In any case, it is possible to estimate a "total" κ factor for the complete data sample by comparing the asymmetries found inside and outside P45. Since there are essentially the same number of periods corresponding to each initial arrangement of polarization orientations, it is expected that the total κ will be much smaller than the individual ones shown in expression (5.24).

Figure 5.19 shows the value of $4m(A_{in} - A_{out})$ for the entire data sample. As before, there is no apparent x dependence. The total averaged value over the x range yields

$$\kappa_{TOTAL} = 1.002 \pm 0.006 \quad (5.25)$$

This value is consistent with zero within the statistical errors, implying that acceptance effects largely cancelled as expected from the combination of several periods. Given this result, we have decided not to introduce any acceptance correction to the final asymmetries, but rather to quote a systematic error originating from the ± 0.006 uncertainty in the value of κ . The detailed values of these errors in each kinematic bin will be given on section 5.5

In addition to the subdivision corresponding to tracks found inside and outside P45, one can try to get independent estimations of the κ factor by splitting the total data sample in different ways

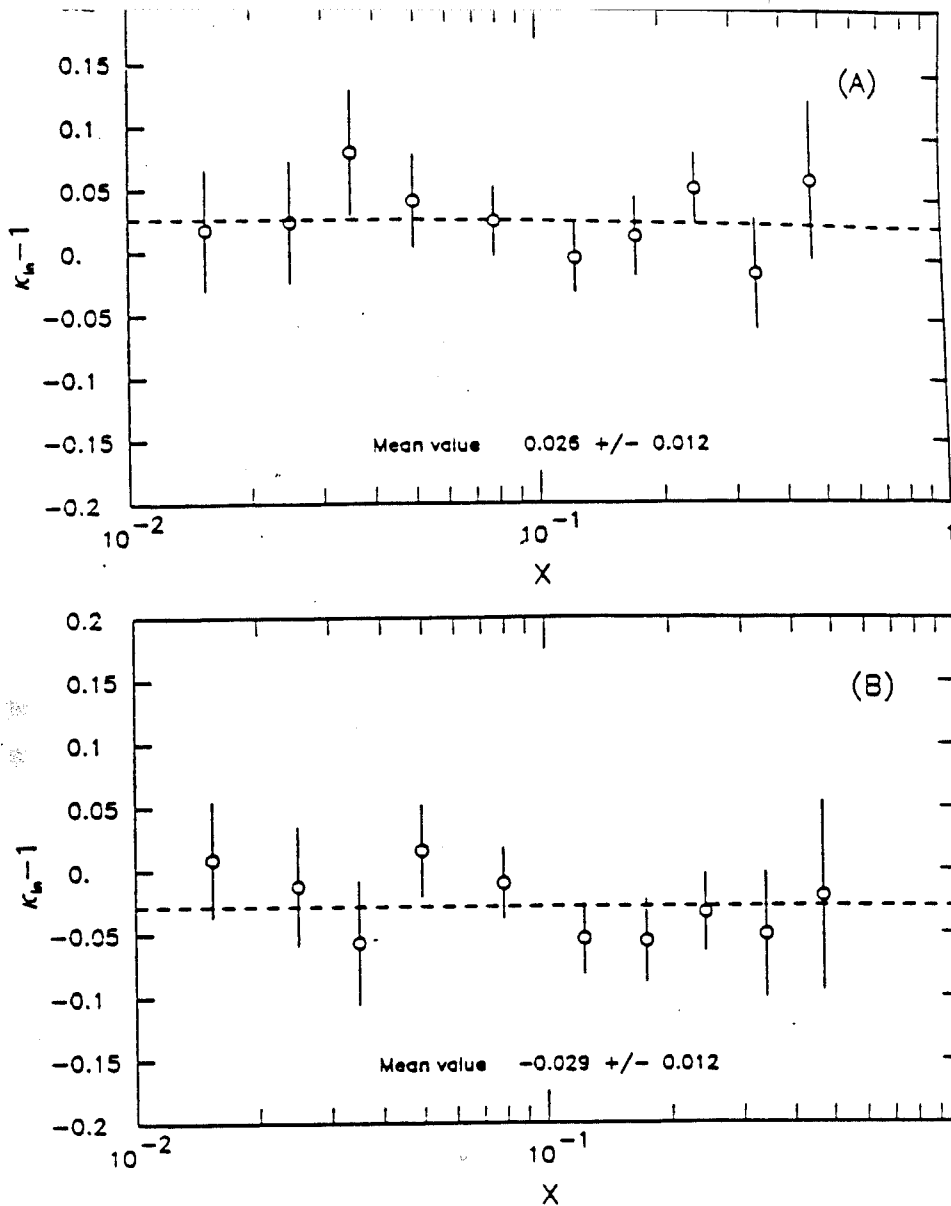


Figure 5.18: An estimation of the κ factor of a single 1984 period. The two plots correspond to opposite starting polarization orientations

such that one half is expected to suffer from acceptance effects much more than the other one. An example of such a splitting consists in subdividing each target half into two quarters and calculating a separate asymmetry for both the pair close to and far away from the intercell gap. The acceptances of the quarters adjacent to the gap should be quite similar, given their proximity in space. On the contrary, the ratio a_+/a_- for the remote subhalves is expected to differ from one by a larger

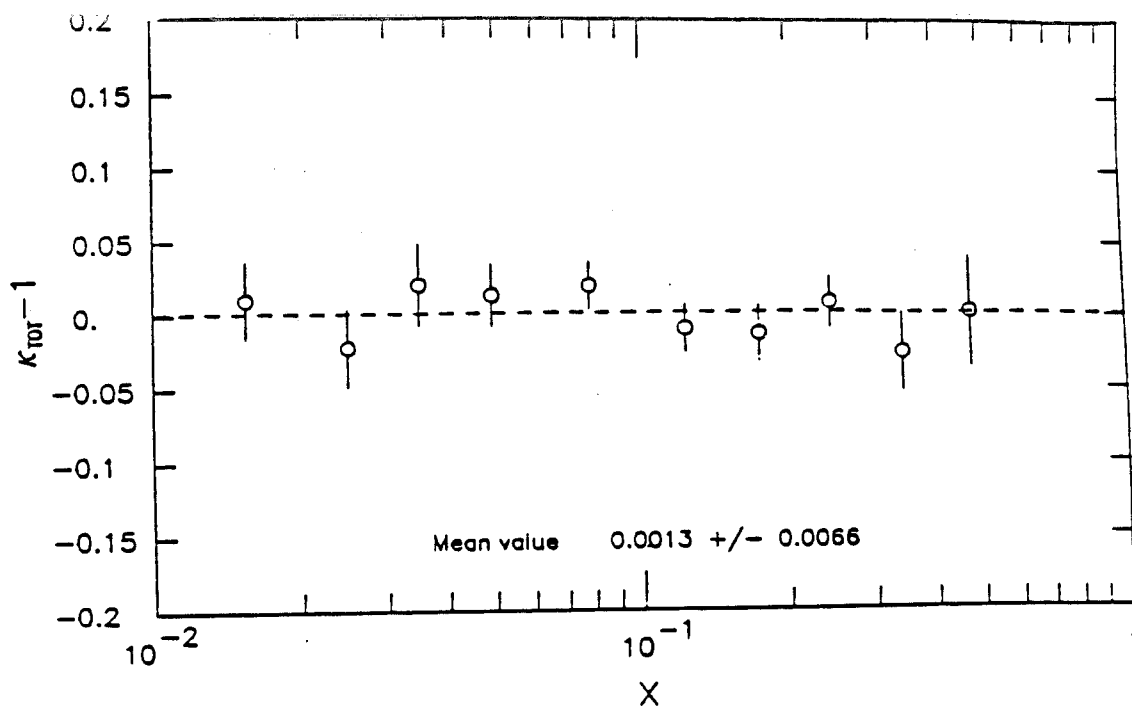


Figure 5.19: Difference between the asymmetries measured inside and outside P45. The result can be interpreted as a measurement of the global κ factor of the experiment

amount. The κ factor can be calculated following a parallel method to the one developed above for case of the P45 cut. A plot of $4m(A_{remote} - A_{adjacent})$ as a function of x shows again no kinematic dependence and the total averaged value yields $\kappa_{TOTAL} = 0.003 \pm 0.006$.